### 2025 S.T. Yau High School Science Award (Asia)

### **Research Report**

#### The Team

Registration Number: Phy-084

Name of team member: Haoyang HUANG

School: Raffles Institution Country: Singapore

Name of supervising teacher: Prof. Nikolai YAKOVLEV

Job Title: Adjunct Associate Professor School: National University of Singapore

Country: Singapore

**Magneto-Impedance Spectrometer for Rotating Magnetic Nanoparticles** 

**Date** 

14 August 2025

#### **Commitments on Academic Honesty and Integrity**

We hereby declare that we

- 1. are fully committed to the principle of honesty, integrity and fair play throughout the competition.
- 2. actually perform the research work ourselves and thus truly understand the content of the work.
- 3. observe the common standard of academic integrity adopted by most journals and degree theses.
- 4. have declared all the assistance and contribution we have received from any personnel, agency, institution, etc. for the research work.
- 5. undertake to avoid getting in touch with assessment panel members in a way that may lead to direct or indirect conflict of interest.
- 6. undertake to avoid any interaction with assessment panel members that would undermine the neutrality of the panel member and fairness of the assessment process.
- 7. observe the safety regulations of the laboratory(ies) where the we conduct the experiment(s), if applicable.
- 8. observe all rules and regulations of the competition.
- 9. agree that the decision of YHSA(Asia) is final in all matters related to the competition.

We declare that declare that this project has been used in the past to participate in the Singapore Science and Engineering Fair (SSEF) in March 2025.

We understand and agree that failure to honour the above commitments may lead to disqualification from the competition and/or removal of reward, if applicable; that any unethical deeds, if found, will be disclosed to the school principal of team member(s) and relevant parties if deemed necessary; and that the decision of YHSA(Asia) is final and no appeal will be accepted.

(Signatures of full team below)

Name of team member: Haoyang HUANG

Name of supervising teacher: Prof. Nikolai YAKOVLEV

Noted and endorsed by

(signature) \

Name of school principal Raffles Institution

AARON LOH Principal

# Magneto-Impedance Spectrometer for Rotating Magnetic Nanoparticles

# Haoyang Huang Phy-084

School: Raffles Institution Mentor: Prof. Nikolai Yakovlev

# Contents

Ab	bstract	1
Ac	cknowledgments	1
1	Introduction	2
2	Engineering Principles	4
	2.1 Mechanical Design	4
	2.2 Electronic Design	5
	2.3 Experimental Control	7
3	Linear Regime	g
	3.1 Effective Field Model	9
	3.2 Particle Size Distributions	10
	3.3 Preliminary Results	11
4	Fokker–Planck Solver	13
	4.1 Governing Equations	13
	4.2 Numerical Solution	14
	4.3 Experimental Verification	17
5	Further Applications	19
	5.1 Weighted-Average Model	19
	5.2 Gelation of Proteins	20
	5.3 Characterization of MNPs	22
6	Conclusion	24
Re	eferences	25
Ap	ppendices	26

# Abstract

We built a fully custom Magneto-Impedance Spectrometer (MIS) that achieves competitive accuracy for frequency-domain phase lag measurements of magnetic nanoparticle suspensions. The MIS uses an Arduino and homemade amplifier to produce digitally generated sinusoidal voltages with an automated frequency sweep up to 820Hz, fed to orthogonal driving coils to produce a 2mT rotating magnetic field. A calibration coil and dual-layer sensing coil geometry that suppresses drive field pickup were also implemented. We verified end-to-end performance by quantifying sub-5% total harmonic distortion across the drive-amplification chain, mapping the field uniformity in the sample zone, and confirming uncertainity due to heating is negligible (sub-1° phase lag error). Preliminary results on low viscosity Newtonian media show promising results for the analytical Effective Field Model (EFM) with a log-normal particle size distribution, but the fits degrade for solutions of higher viscosity. Thus, we implemented a more robust theoretical framework that resolves high field and frequency nonlinearities via a numerical Fokker-Planck (FP) solver while accounting for parallel Brownian and Néel relaxation pathways; this model corrects the systematic overprediction observed at higher viscosities. Further insights are presented where we tested the gelation of proteins namely egg white, for which we derived our own Weighted Average (WA) Model to determine gelation temperature and gel porosity. Our machine has notable potential applications ranging from precise quality control of IV fluids and injectables to real-time control of food gel consistency and texture.

Keywords: Magnetic Nanoparticles, Magnetic Impedance Spectroscopy, Micro-viscosity, Rotating Magnetic Fields, Gelation of Proteins

# Acknowledgments

I would like to express my heartfelt appreciation to my mentor Prof. Nikolai Yakovlev for his invaluable support and guidance on this project, as well as the NUS Science Research Program for allowing me to access the NUS Physics lab and resources for this project. Also, I would like to thank Lin Jiarui, Jae Lee, and Wang Yunze for their help and advice.

# 1 Introduction

In recent years, magnetic nanoparticles (MNPs) have seen extensive and promising applications due to the possibility of manipulating them with an external magnetic field. They have proven useful in a diverse array of domains including cancer therapy, environmental studies and substrate analysis in material science [1]. This is attributed to their small size, as well as a highly responsive dipole moment when stimulated with external magnetic fields [2], which gives rise to precise detection capabilities, making MNPs particularly useful as miniature sensors to reveal microscopic information about a system. In our study, we are interested in creating a device capable of accurately measuring the micro-viscosity of fluid samples by using MNPs as probes [3]. Currently, two of the most widely used tools are the rotational viscometer and dynamic light scattering (DLS) microrheology systems. A rotational viscometer measures torque on a rotating spindle immersed in the fluid, and is common in laboratories and various industries due to its reliability. However, it requires direct contact with the sample, a relatively large volume for spindle immersion, and is less suited to very small and turbid samples. DLS microrheology works by tracking the Brownian motion of tracer particles using laser light scattering to infer microviscosity. It can handle small volumes and gives micro-timescale information, but is costly and requires optically clear samples with minimal turbidity [4].

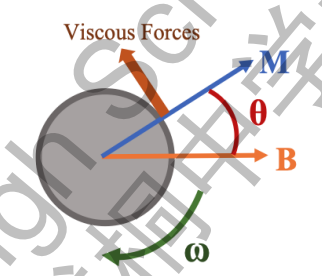


Figure 1: Dynamics of an MNP in a rotating B field.

Therefore, we engineered our very own Magneto-Impedance Spectrometer (MIS) from the ground up to address these problems in a creative way. The MIS works by applying an external rotating magnetic (B) field that rotates the MNPs suspended in a fluid. Its magnetization vector will lag behind that of the rotating B field (Fig 1) by an angle  $\theta$  due to viscous forces and thermal agitation which hinder rotation. Our instrument measures the phase lag  $\theta$  between magnetic field and magnetization vector and provides us with a phase lag spectra, hence the name Magneto-Impedance Spectrometer.

Instrument	Cost (USD)	Sample size (mL)	Accuracy
Viscometer	2,000-10,000	$\gtrsim 10$	1-2%
DLS	40,000-100,000	$\lesssim 1$	2–5%
Our MIS	30-50	$\lesssim 1$	2–8%

In comparison, our MIS is much cheaper, non-contact, works with small or opaque samples, and offers competitive accuracy in the range of 2–8% for Newtonian standards, with the potential to characterise heterogeneous samples where conventional tools cannot operate effectively. As of the time of this study, no other similar MIS system is commercially available.

In this report, we first describe how our spectrometer was constructed and its underlying principles in Section 2. In Section 3, we outlined the analytical Effective Field Model (EFM) from prior literature and explained how we accounted for the polydispersity of our own particle sizes, before conducting tests on simple Newtonian media of distilled water and 5% Glycerin solution that yielded promising results. However, subsequent tests on solutions of higher viscosity produced bad fits for the EFM. Thus, in Section 4, we implemented a more rigorous Fokker-Planck Solver that accounted for both Brownian and Néel Relaxation as well, which provided us with compelling fits for solutions of higher viscosity. Finally, in Section 5, we derived our own Weighted Average (WA) model for more complex, non-Newtonian media, and used it to characterize properties of gels such as porosity and gelation temperature, and spot aggregation of MNPs.

# 2 Engineering Principles

## 2.1 Mechanical Design

A rotating magnetic field of variable frequency is produced externally by the two pairs of driving coils that surround the test chamber, where our samples containing MNPs are placed. A three-dimensional schematic of the coils of our MIS is shown in Fig. 2a. The circuitry is designed such that the current passing through the X and Y driving coils are 90-degrees out of phase with each other. This ensures that the resultant magnetic field rotates smoothly, allowing for more accurate analysis of the magnetic response by the MNPs. Four pairs of sensing coils are contained within the 3-D printed cuboidal scaffold which detect the magnetic response of the MNPs within the sample. Driving coils, each of appropriate dimensions and resistance  $220\,\Omega$ , were made ourselves using an automated winding system.

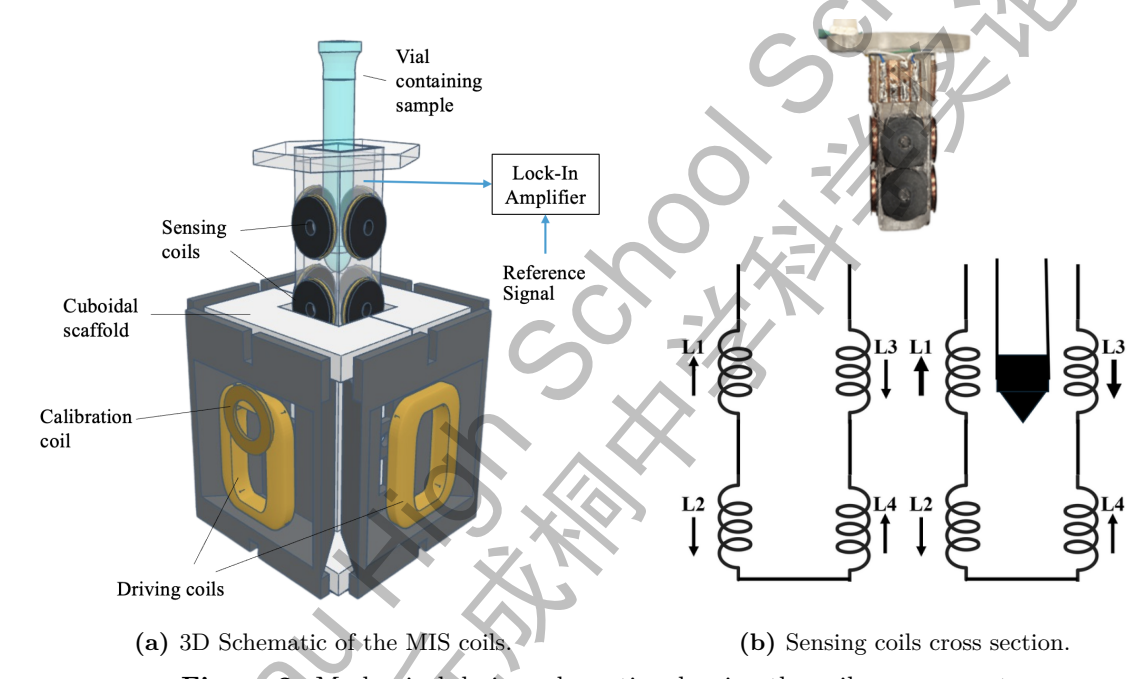


Figure 2: Mechanical design schematics showing the coil arrangement.

The sensing coils were obtained from an electronics manufacturer, with the pairs of X and Y sensing coils connected on opposite sides of the scaffold. The sensing coils are placed in pairs where the bottom sensing coil is wired in opposite polarity to the top (Fig. 2b); the induced electrical signals due to the rotating field in the top and bottom layers cancel out when no sample is present. When a sample is inserted, it is aligned only with the top coil, inducing an electric signal that is attributed only to the MNP response and easily measurable by the Lock-In Amplifier (LIA). A calibration coil is also installed in series with the X coils. It serves two purposes: to determine the baseline zero error of the system by simulating a sample with zero phase lag, and for selection of an appropriate phase offset for our LIA. Viscosity is also extremely temperature sensitive, and we adopted a negative pressure airflow setup such that cool air will reach the coils where the sample is contained first, before passing over circuit components and getting expelled by a fan.

#### 2.2 Electronic Design

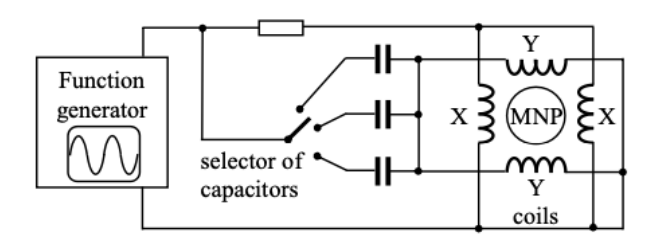


Figure 3: Initial driving system using capacitive circuit.

The generation of oscillating voltages is traditionally achieved using a function generator. However, standard function generators only provide a single oscillating voltage output, not to mention they are bulky and costly. To generate orthogonal components, a circuit incorporating capacitors in series with coils (Fig. 3) was initially used. The performance of the circuit depends on the capacitance value at each frequency. If the capacitance is excessively high, the phase shift of the current approaches zero. Conversely, if the capacitance is too low, the phase shift increases but the amplitude in the Y-coils decreases, necessitating the use of a resistor in series with the X-coils to stabilize performance. Therefore, achieving optimal operation at each frequency is an arduous and delicate process. Moreover, constant adjustments to the capacitors to change frequency made the system unstable and very prone to human error during operation.

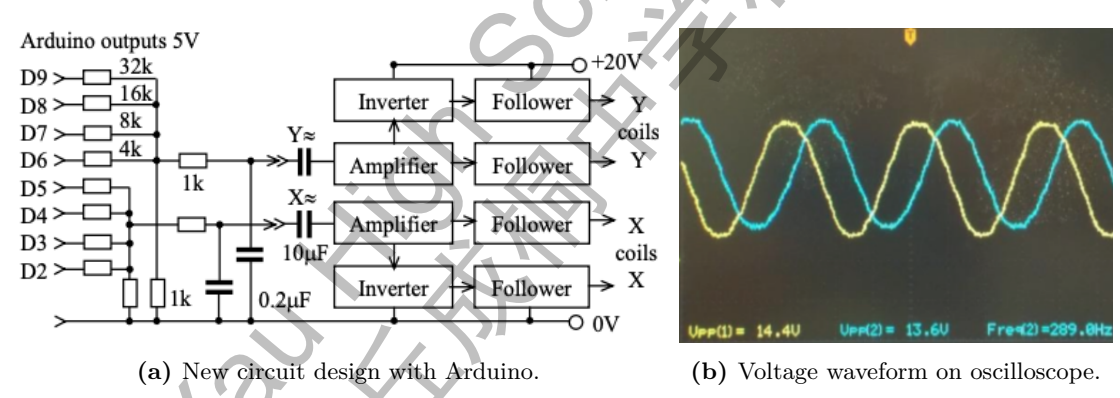


Figure 4: Our own driving system for the MIS.

Thus, we decided to build our own custom electronics for our MIS prototype, using an Arduino microprocessor to achieve the digital generation of sinusoidal voltages. The microprocessor outputs digital signals of either 0V or 5V, which are subsequently converted into a 15-level analogue voltage through voltage summation using a resistor network. Identical resistor networks are implemented for both the X-coils and Y-coils. The timing of output bits is precisely controlled by the program to correspond to one-quarter of the period at each frequency. The generation of sinusoidal signals using the Arduino Uno is implemented in two stages. First, the microcontroller constructs an array of 360 elements corresponding to 360 degrees in a full periodic cycle, with values ranging from 0 to 15, calculated using the formula:

element(n) = int 
$$\left(7.5 - 7.5\cos\left(\frac{n\pi}{180}\right)\right)$$
 (1)

Subsequently, the program iteratively selects every second, third, fourth, or higher indexed el-

ement, depending on the desired frequency. Each selected value is converted into four bits and transmitted to outputs D2 through D5 to produce the X-signal. Simultaneously, the program selects the value located 90 indices ahead in the array, converts it into bits, and sends it to outputs D6 through D9 to generate the Y-signal. We then output the integer value in a binary format to determine if it should output HIGH or LOW on the digital output pin. These signals are passed through a Digital to Analogue Circuit (DAC) and capacitors of 200nF to create smoothened sine waves before they are subsequently amplified to a voltage of 20V and a current of 0.1A using voltage and current followers to drive the main coils. This bespoke approach eliminates the need to manually swap capacitors and adjust circuitry for each frequency, minimizing human error and ensuring more stable phase and amplitude control.

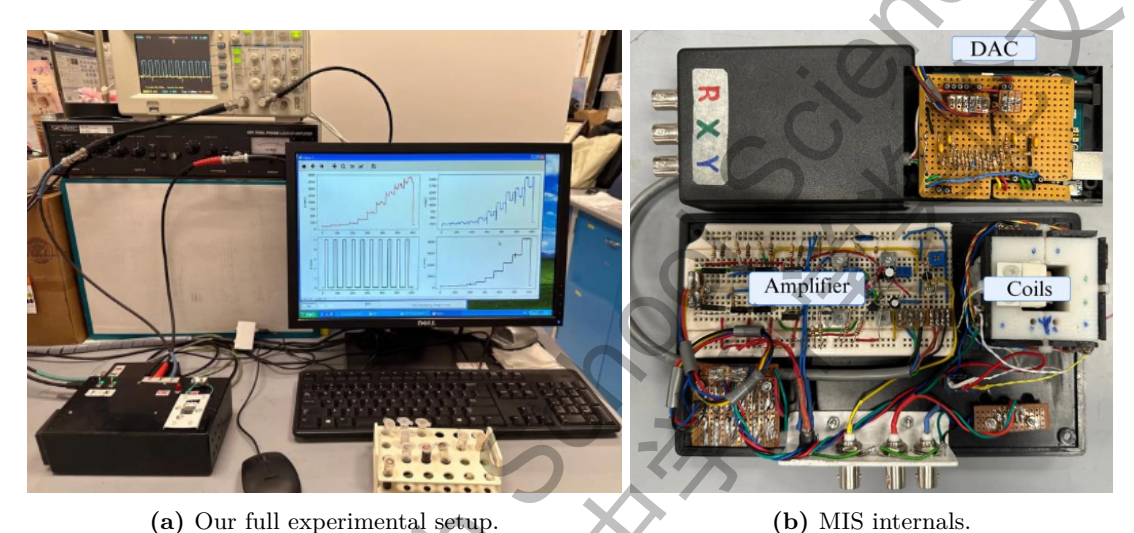


Figure 5: The fully assembled MIS system.

To process the response of the MNPs, the sensing coils are connected to a dual-phase Lock-In Amplifier (LIA). We take a reference signal from the current going to the X-driving coils which is in-phase with the rotating magnetic field. The LIA also amplifies the weak induced emf from the sensing coils and isolates the component in or out of phase with the field whilst filtering out noise, ensuring that the phase lag measurements are accurate. Lastly, our Arduino program also digitizes and collates the LIA output signals for analysis, after which the phase lag angle  $\theta$  can be extracted for modeling.

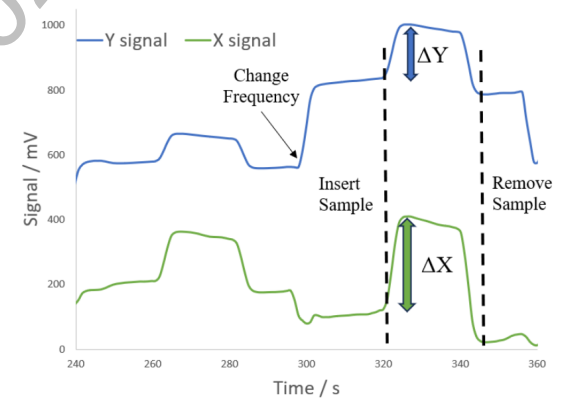


Figure 6: Real-time signal changes during measurement.

Data acquisition is done by starting the Arduino program, which begins the frequency sweep at the lowest band of 30Hz all the way to 820Hz. We wait 20s for the frequency to stabilize, then proceed to insert the sample vial for 20s before removal. After removal, we wait another 20s before the next frequency change every 60s (Fig. 6). The phase lag  $\theta$  can then be calculated using the equation:

 $\tan(\theta) = \frac{\Delta Y}{\Delta X} \tag{2}$ 

where  $\Delta Y \& \Delta X$  are the increments in the detected signals. A prewritten excel script is used to convert the raw signals into phase lag values using Eqn. 2. The phase lag versus frequency spectra for various samples are depicted in Sections 3.3, 4.3, 5.2, and 5.3.

# 2.3 Experimental Control

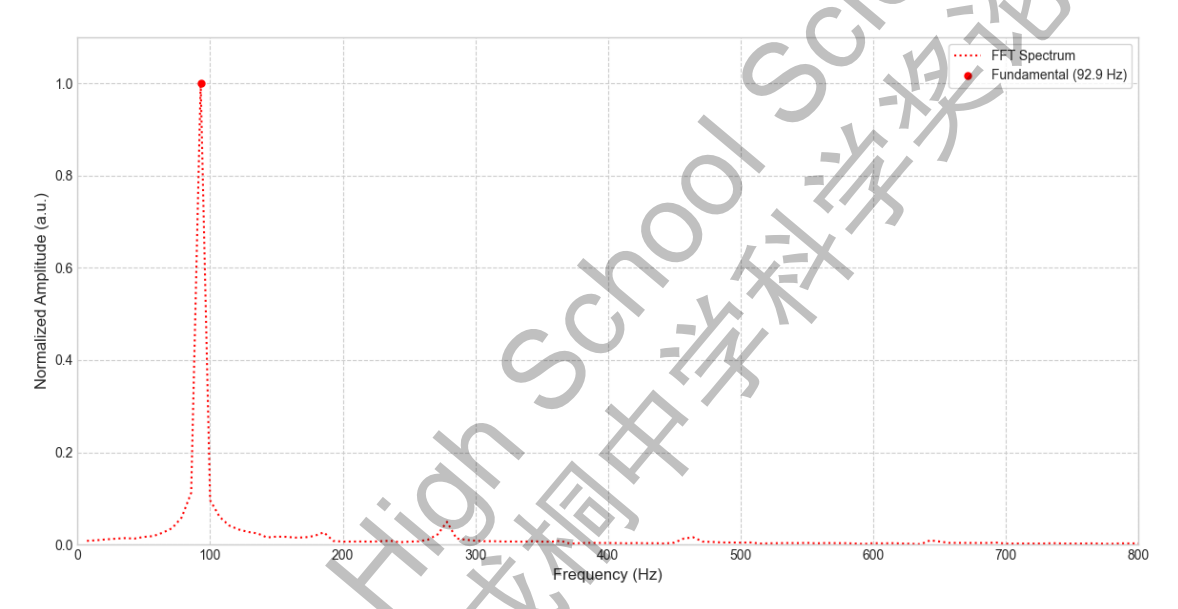
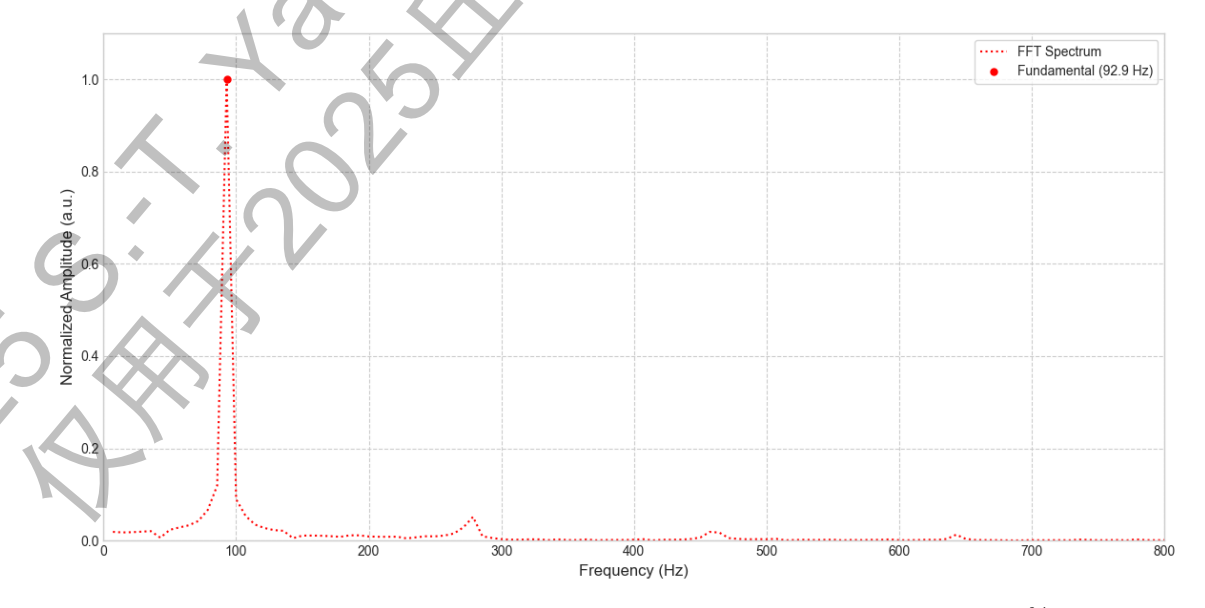


Figure 7: FFT of the voltages applied across the X coils,  $THD_X = 4.86\%$ .



**Figure 8:** FFT of the voltages applied across the Y coils,  $THD_Y = 4.58\%$ .

To quantify the purity of our digitally generated signals, we computed the Fast Fourier Transform (FFT) of the coil-drive voltage (peak normalized to 1) and evaluated the total harmonic distortion (THD) as the RMS of the harmonic amplitudes relative to the fundamental. The resulting THD is  $THD_X \approx 4.86\%$  and  $THD_Y \approx 4.58\%$ . Some distortion is inherent to digitally generated waveforms, which is the frequency of digitising,  $9f_0$  in our case. The presence of other small odd harmonics (e.g.,  $3f_0$ ) are due to distortion in the amplifier/filter when output voltage approaches zero or the power supply voltage 24V rather than the DAC itself [6]. Crucially, the absence of even harmonics proves that our waveform is symmetric. Moreover, the dual-phase LIA will only extract the signal of the MNPs at the fundamental frequency  $f_0$  and reject higher harmonics. Thus, the <5% THD levels have negligible influence on the reported in-phase and quadrature responses at  $f_0$ .

To characterise the intrinsic phase offset of the magneto-impedance spectrometer (MIS), a small calibration coil (see Fig. 2a) is wired in series with the X-driving coil and gated by a manual switch. When the switch is open, the MIS operates normally, sensing the sample's phase lag. When the switch is closed, the calibration coil carries the same driving current but presents zero phase lag  $\theta$ , effectively simulating an ideal sample. Under this condition, the LIA should register a phase difference of exactly 0°. Any nonzero reading, is therefore the zero error of the system. In practice we find  $\theta_{zero} < 6^{\circ}$  and this offset is subtracted from all subsequent sample measurements to yield true phase lags.

Magnetic field uniformity was assessed by passing a steady DC current (equal to the peak current during AC mode) through the X-driving coils then using a calibrated Hall probe to take measurements of the magnetic field strength at the geometric center and six symmetrically displaced points corresponding to the midpoints of the sample vial's bounding volume (total 7 points). The vial has a 10 mm diameter and the sample occupies around 12 mm in height. The mean field strength was 2.0mT, with peak-to-peak non-uniformity verified to be under 6%.

Because liquid viscosity typically follows an Arrhenius-type dependence, its exponential sensitivity to 1/T means that temperature is the largest contributor to propagated error. In our MIS, the presence of many coils surrounding the sample might introduce unwanted heat skewing the results. To prevent this, we installed a fan that expels hot air out of the MIS. To verify if this is adequate, we logged the temperature changes of our sample by sticking a digital thermometer, the ThermoPro-TP610, into a sample containing distilled water and measuring the temperature fluctuations within a 10-min run. We roughly estimated the influence of temperature drift and thermometer accuracy on the measured phase lag using our theoretical model presented in Section 3.1, which came out to be that the worst-case temperature-induced phase uncertainty is  $\lesssim 1^{\circ}$  (see Appendix B) at the relaxation peak, and smaller elsewhere. We can thus use a constant T assumption with confidence in our model's predictive power.

# 3 Linear Regime

#### 3.1 Effective Field Model

One model of predicting the magnetic response is the analytical Effective Field Model (EFM) [7]. In general, this model yields accurate results under the assumption that the system must operate in the linear response regime with low field amplitudes and low frequencies. We model a dilute ensemble of non-interacting, single-domain magnetic nanoparticles in a Newtonian fluid driven by a circularly-polarised field of amplitude B = 2mT and angular frequency  $\omega$ . We define the ratio magnetic energy of an MNP to the thermal energy

$$\xi = \frac{mB}{k_B T}$$

where  $m = M_s V_c$  is magnetic moment of a single particle ( $M_s = 2.75 \times 10^5$  A/m is the saturation magnetization,  $V_C$  is the volume of the magnetite core of the MNP),  $k_B$  Boltzmann's constant and T the absolute temperature. We introduce the Langevin function

$$L(\xi) = \coth(\xi) - \frac{1}{\xi}$$

which describes the average alignment of magnetic dipoles in an external B-field, accounting for thermal agitation. The characteristic Brownian (rotational) relaxation time is

$$\tau_B = \frac{3 \, \eta \, V_H}{k_B \, T}$$

with  $\eta$  the fluid viscosity and  $V_H$  the particle's hydrodynamic volume. In the presence of a finite field the effective perpendicular relaxation time becomes

$$\tau_{\perp} = \tau_B \, \frac{2 \, L(\xi)}{\xi - L(\xi)}$$

reflecting the fact that strong fields hinder random reorientation. The complex reduced magnetisation components  $M'(\omega)$  (in-phase) and  $M''(\omega)$  (out-of-phase) then follow the forms

$$M'(\omega) = \frac{L(\xi)}{1 + (\omega \, \tau_{\perp})^2},\tag{3}$$

$$M''(\omega) = \frac{L(\xi)\,\omega\,\tau_{\perp}}{1 + \left(\omega\,\tau_{\perp}\right)^2},\tag{4}$$

so that the phase lag  $\theta(\omega)$  between the magnetisation and the drive satisfies

$$\tan \theta(\omega) = \frac{M''(\omega)}{M'(\omega)} = \omega \,\tau_{\perp} = \omega \,\tau_{B} \,\frac{2 \,L(\xi)}{\xi - L(\xi)} \tag{5}$$

from which we can extract the desired phase lag spectrum  $\theta(\omega)$ .

### 3.2 Particle Size Distributions

Real-world MNP samples are inherently polydisperse, meaning they contain a distribution of core and hydrodynamic diameters rather than a single, uniform size. Because the particle magnetic moment scales with core volume, and Brownian relaxation time scales with hydrodynamic diameter neglecting this distribution can produce large discrepancies between theory and experiment, especially in viscous media [5]. The manufacturer's specification sheet (Appendix A) provide us with a Transmission Electron Microscopy (TEM) histogram with the core size distribution. We model the core diameters,  $d_c$ , with a log-normal probability density function (PDF):

$$f_c(d_c) = \frac{1}{d_c \sigma_{\ln} \sqrt{2\pi}} \exp\left[-\frac{(\ln d_c - \mu_{\ln})^2}{2\sigma_{\ln}^2}\right]$$
 (6)

where the logarithmic parameters are obtained from the manufacturer's TEM statistics,  $\mu_{\rm arith} = 16.1\,{\rm nm}$  and  $\sigma_{\rm arith} = 4.8\,{\rm nm}$ , via

$$\sigma_{
m ln} = \sqrt{\ln(1+\sigma_{
m arith}^2/\mu_{
m arith}^2)}, \qquad \mu_{
m ln} = \ln(\mu_{
m arith}) - rac{1}{2}\sigma_{
m ln}^2$$

For the present sample these give  $\sigma_{\rm ln} \simeq 0.292$  and  $\mu_{\rm ln} \simeq 2.736$ . The continuous PDF is discretised into N=7 representative core diameters  $d_{c,i}$ , and the probability weight of each bin is obtained by integrating  $f_c(d_c)$  over the bin. The complex magnetisation of the ensemble is then formed as a weighted average,

$$\langle M(\omega) \rangle = \sum_{i=1}^{N} w_i M(\omega, d_{c,i})$$
 (7)

where  $M(\omega, d_{c,i})$  is the single–particle response at angular frequency  $\omega$ .

The manufacturer's specification sheet only lists a single mean hydrodynamic diameter rather than a full distribution. The simplest physically consistent way to endow the hydrodynamic diameters with a distribution is to assume that each magnetic core is coated by a uniform, non-magnetic shell of thickness t taken directly from the specification sheet. We then map every core diameter to a hydrodynamic diameter through

$$d_h = d_c + 2t \tag{8}$$

so that the hydrodynamic PDF is simply the core PDF translated by 2t. Because the shift leaves the probability weights unchanged, the same set of  $w_i$  is used when hydrodynamic terms such as the Brownian relaxation time are evaluated; only the diameter entering those terms is replaced by  $d_{h,i} = d_{c,i} + 2t$ . The critical assumption of a constant shell thickness, t, across the entire core size distribution is justified by the uniform surface chemistry imparted during synthesis, which results in a consistent surfactant coating and bound solvent layer irrespective of minor variations in core size [8].

#### 3.3 Preliminary Results

We begin testing the MIS on simple Newtonian fluids of distilled water and  $\approx 10\%$  dilute glycerin solutions. The samples are prepared in 2ml conical tubes by adding around 1ml of sample followed by 50 µl of NMP suspension obtained from nanoComposix, characteristics of which can be found in Appendix A. The phase spectrum provided by the MIS is shown below. Our optimizer fits the analytical EFM with the parameter of viscosity to the data points.



Figure 9: Pictures of samples (water and Glycerin solution.)

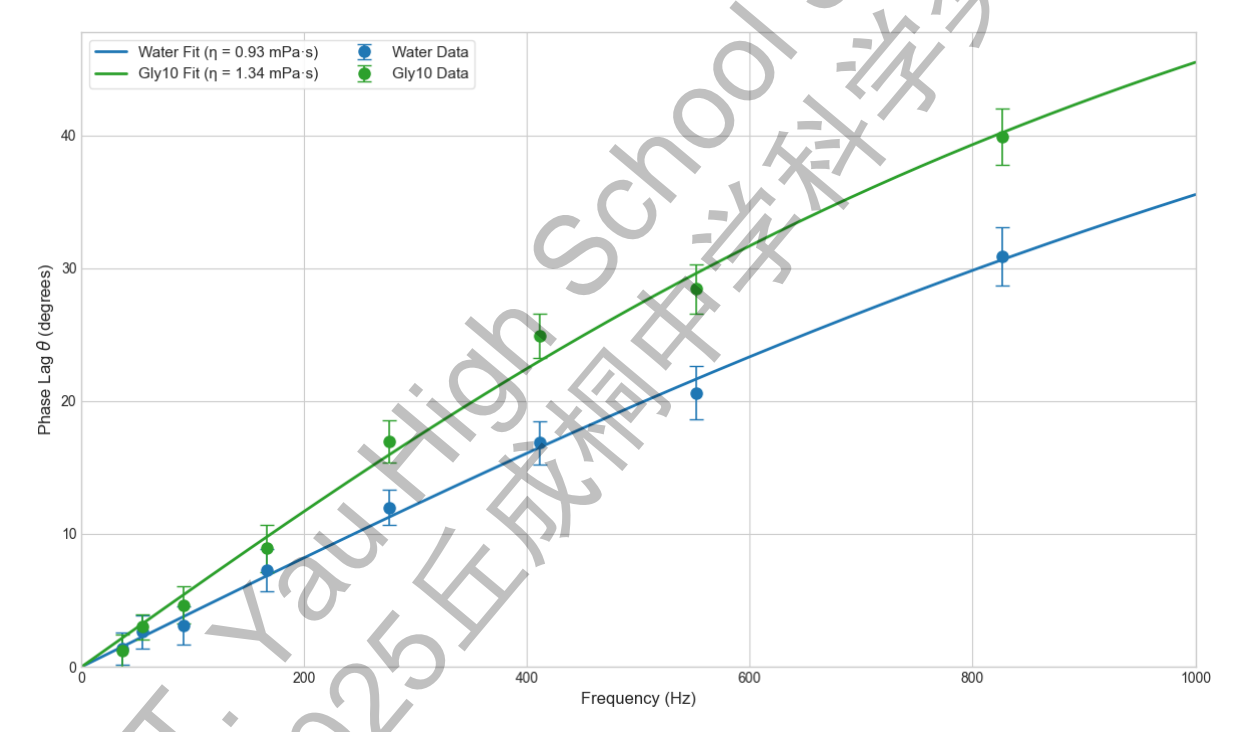


Figure 10: Phase Spectrum for Distilled Water and Glycerin 10% Solution.

Sample	Fit (mPa·s)	Actual (mPa·s)	Fit $R^2$
Water	0.93	0.95	0.995
Gly 10%	1.35	1.28	0.992

Using the analytical Effective Field model with a log-normal core and hydrodynamic PSD, we obtain a good agreement with the measured phase spectra over 0-1000 Hz for distilled water and 10% glycerin as shown in Fig. 10. We meet a baseline verification that the phase lag increases with frequency, and the measured viscosity does indeed increase when we introduce Glycerol. The fitted viscosities are consistent with values measured by a commercial viscometer. The goodness of fit measured by  $R^2$  is high in both cases, and the residuals show no systematic

trend across frequency. The frequency shift from water to 10% glycerin follows the expected  $1/\eta$  scaling, indicating Brownian–dominated relaxation in this band. Taken together, these results support the adequacy of modeling hydrodynamic sizes by translation of the core distribution, which preserves particle—wise correlation between magnetic moment and drag while introducing no additional fit parameters, and they validate the MIS for viscosity retrieval in low–to–moderate viscosity Newtonian media. We conclude that the Effective Field model works very well in the linear regime.

However, upon conducting further tests on higher concentrations of Glycerin solution, 30% and 60%, we notice that the fits degrade most noticeably in the upper portion of the 0–1000 Hz band as shown later on in Fig. 12 and 13. Furthermore, our theory line has a consistent trend of overpredicting at high frequencies. We attribute this to two physical effects becoming significant: first, as viscosity increases, the Brownian time  $\tau_B \propto \eta$  lengthens, bringing a nonnegligible fraction of particles into a regime where the Néel relaxation (explained later)  $\tau_N$  and  $\tau_B$  are comparable; the current model solely accounts for Brownian relaxation. Second, at higher driving frequencies or larger field strengths, the response departs from the linear Debye form [7], with these discrepancies growing in the nonlinear regime. This motivates us to develop a more physically complete and rigorous model.

# 4 Fokker-Planck Solver

The analytical models break down at high field strengths and frequencies where deterministic torques severely distort the distribution [7]. Thus, we implement a full Fokker-Planck (FP) approach that captures the full steady-state magnetization probability distribution  $W(\theta, \phi)$ , including higher-order spherical harmonic modes and asymmetric broadening that arise from field-dependent nonlinearities. The work here is based on research by Yoshida *et al.* (2012).

Here we also introduce Néel relaxation, the internal process in which the MNP's magnetic moment rotates within the crystal lattice to realign with the external magnetic field, instead of the physical rotation of the entire MNP for Brownian. We conventionally use the effective relaxation time ( $\tau_{\rm eff}$ ) which considers both mechanisms in parallel:

$$\frac{1}{\tau_{\text{eff}}} = \frac{1}{\tau_B} + \frac{1}{\tau_N} \tag{9}$$

where  $\tau_B = \frac{3\eta V_H}{k_B T}$  is the Brownian relaxation time,  $\tau_N = \tau_0 \exp\left(\frac{K V_C}{k_B T}\right)$  is the Néel relaxation time (independent of viscosity) where  $\tau_0 = 2.5 \times 10^{-9}$  s is the attempt time,  $K = 3.6 \times 10^4 \text{ J/m}^3$  is the material-dependent magnetic anisotropy constant characterised via VSM Magnetometry, and all other parameters are as defined previously in Section 3.1. For solutions of low viscosity,  $\tau_B << \tau_N$ , and Eqn. 9 reduces to the simple Brownian-only form.

## 4.1 Governing Equations

We start by writing the FP equation for the probability distribution function  $W(\theta, \phi, t)$  of the magnetic moment's orientation. For a magnetic field  $\mathbf{B}_{RMF}(t)$  of amplitude B rotating in the xy-plane with angular frequency  $\omega$  (potential energy  $E = -mB\sin\theta\cos(\omega t - \phi)$ ):

$$2\tau_{\text{eff}} \frac{\partial W}{\partial t} = \frac{1}{k_B T} \left( \nabla^2 E \right) W + \frac{1}{k_B T} \nabla E \cdot \nabla W + \nabla^2 W \tag{10}$$

Since we are looking for the steady-state behavior, we move to a coordinate system  $(x_r, y_r, z)$  that rotates with the magnetic field to remove the time dependency of the equation. In this frame, the distribution function  $W_r(\theta, \phi_r)$  becomes stationary  $(\partial W_r/\partial t = 0)$ . The function  $W_r$  is expanded into a series of spherical harmonics:

$$W_r(\theta, \phi_r) = \sum_{n=0}^{N} \sum_{m=-n}^{n} b_{n,m} Y_n^m(\theta, \phi_r) = \sum_{n=0}^{N} \sum_{m=-n}^{n} b_{n,m} P_n^{|m|}(\cos \theta) e^{im\phi_r}$$
(11)

where  $b_{n,m}$  are the complex coefficients to be determined, and  $P_n^{|m|}$  are the associated Legendre polynomials. Since  $W_r$  must be real, the coefficients satisfy the condition  $b_{n,-m} = (-1)^m b_{n,m}^*$ . The series is truncated at a sufficiently large integer N for numerical accuracy. The key is to solve for the coefficients  $b_{n,m}$ . For numerical implementation, it is convenient to separate the

real and imaginary parts of the coefficients. We define a vector of coefficients for each order n:

$$C_{n} = \begin{bmatrix} c_{n,0} \\ c_{n,1} \\ \vdots \\ c_{n,n} \end{bmatrix} \quad \text{where} \quad c_{n,m} = \begin{bmatrix} \operatorname{Re}(b_{n,m}) \\ \operatorname{Im}(b_{n,m}) \end{bmatrix}$$
(12)

Here,  $C_n$  is a column vector of size  $2(n+1) \times 1$ . Using recurrence relations and the orthogonal properties of the associated Legendre functions, we obtain the following equation:

$$\mathbf{Q}_{n,m}\mathbf{c}_{n,m} + \mathbf{R}_{n,m}^{+-}\mathbf{c}_{n+1,m-1} + \mathbf{R}_{n,m}^{++}\mathbf{c}_{n+1,m+1} = \mathbf{S}_{m,m}^{--}\mathbf{c}_{n-1,m-1} + \mathbf{S}_{n,m}^{-+}\mathbf{c}_{n-1,m+1}$$
(13)

The block matrices in Equation 13 are defined as follows:

$$\mathbf{Q}_{n,m} = \begin{bmatrix} 2n(n+1) & 4\tau_{\text{eff}}m\omega \\ -4\tau_{\text{eff}}m\omega & 2n(n+1) \end{bmatrix}$$
 (14)

$$\mathbf{R}_{n,m}^{+-} = \begin{cases} -\xi \frac{n}{2n+3} \mathbf{I}_2 & (m \ge 1) \\ \mathbf{0} \mathbf{I}_2 & (m = 0) \end{cases}$$
 (15)

$$\mathbf{R}_{n,m}^{++} = \begin{cases} \xi \frac{n(n+m+1)(n+m+2)}{2n+3} \mathbf{I}_2 & (m \ge 1) \\ 2\xi \frac{n(n+1)(n+2)}{2n+3} & 0 \\ 0 & 0 \end{cases} \quad (m = 0)$$
 (16)

$$\mathbf{S}_{n,m} = \begin{cases} \xi \frac{n+1}{2n-1} \mathbf{I}_2 & (m \ge 1) \\ \mathbf{0} \mathbf{I}_2 & (m = 0) \end{cases}$$
 (17)

$$\mathbf{S}_{n,m}^{-+} = \begin{cases} -\xi \frac{(n+1)(n-m-1)(n-m)}{2n-1} \mathbf{I}_2 & (m \ge 1) \\ -2\xi \frac{(n-1)n(n+1)}{2n-1} & 0 \\ 0 & 0 \end{cases} \quad (m = 0)$$
 (18)

The diagonal blocks  $\mathbf{Q}_{n,m}$  encode the self-interaction at order n being rotational diffusion and magnetic drift. The off-diagonal couplings  $R_{n,m}$  and  $S_{n,m}$  transfer information to neighboring degrees through the field-induced torque proportional to  $\xi$ . The superscripts '++', '+-', etc., denote the coupling from (n,m) to (n+1,m+1) and (n+1,m-1) respectively, and vice versa.

### 4.2 Numerical Solution

The solution to Eqn. 13 (the vectors of  $c_{n,m}$ ) can be obtained via the following recurrence relation:

$$\mathbf{Q}_n \mathbf{C}_n + \mathbf{R}_n \mathbf{C}_{n+1} = \mathbf{S}_n \mathbf{C}_{n-1} \tag{19}$$

where each matrix is defined as:

$$\mathbf{Q}_{n} = \begin{bmatrix}
\mathbf{Q}_{n,0} & \mathbf{0} & \cdots & \mathbf{0} \\
\mathbf{0} & \mathbf{Q}_{n,1} & \cdots & \mathbf{0} \\
\vdots & \vdots & \ddots & \vdots \\
\mathbf{0} & \mathbf{0} & \cdots & \mathbf{Q}_{n,n}
\end{bmatrix}$$

$$\mathbf{R}_{n} = \begin{bmatrix}
\mathbf{0} & \mathbf{R}_{n,0}^{++} & \mathbf{0} & \cdots & \mathbf{0} \\
\mathbf{R}_{n,1}^{+-} & \mathbf{0} & \mathbf{R}_{n,1}^{++} & \cdots & \mathbf{0} \\
\vdots & \ddots & \ddots & \ddots & \vdots \\
\mathbf{0} & \cdots & \mathbf{R}_{n,n}^{+-} & \mathbf{0} & \mathbf{R}_{n,n}^{++}
\end{bmatrix}$$

$$\mathbf{S}_{n} = \begin{bmatrix}
\mathbf{0} & \mathbf{S}_{n,0}^{-+} & \mathbf{0} & \cdots & \mathbf{0} \\
\mathbf{S}_{n,1}^{--} & \mathbf{0} & \mathbf{S}_{n,1}^{-+} & \cdots & \mathbf{0} \\
\vdots & \ddots & \ddots & \ddots & \vdots \\
\mathbf{0} & \cdots & \mathbf{0} & \mathbf{0} & \mathbf{0}
\end{bmatrix}$$

$$\mathbf{S}_{n} = \begin{bmatrix}
\mathbf{0} & \mathbf{S}_{n,0}^{-+} & \mathbf{0} & \cdots & \mathbf{0} \\
\mathbf{S}_{n,1}^{--} & \mathbf{0} & \mathbf{S}_{n,1}^{-+} & \cdots & \mathbf{0} \\
\vdots & \ddots & \ddots & \ddots & \vdots \\
\mathbf{0} & \cdots & \mathbf{0} & \mathbf{0} & \mathbf{0}
\end{bmatrix}$$

$$\mathbf{C}_{n} = \begin{bmatrix}
\mathbf{0} & \mathbf{S}_{n,0}^{-+} & \mathbf{0} & \cdots & \mathbf{0} \\
\mathbf{S}_{n,1}^{--} & \mathbf{0} & \mathbf{S}_{n,1}^{-+} & \cdots & \mathbf{0} \\
\vdots & \ddots & \ddots & \ddots & \vdots \\
\mathbf{0} & \cdots & \mathbf{0} & \mathbf{0} & \mathbf{0}
\end{bmatrix}$$

$$\mathbf{C}_{n} = \begin{bmatrix}
\mathbf{0} & \mathbf{S}_{n,0}^{-+} & \mathbf{0} & \cdots & \mathbf{0} \\
\mathbf{S}_{n,1}^{--} & \mathbf{0} & \mathbf{S}_{n,1}^{-+} & \cdots & \mathbf{0} \\
\vdots & \ddots & \ddots & \ddots & \vdots \\
\mathbf{0} & \cdots & \mathbf{0} & \mathbf{0} & \mathbf{0}
\end{bmatrix}$$

$$\mathbf{C}_{n} = \begin{bmatrix}
\mathbf{0} & \mathbf{0} & \mathbf{0} & \mathbf{0} & \mathbf{0} & \mathbf{0} \\
\mathbf{0} & \mathbf{0} & \mathbf{0} & \mathbf{0} & \mathbf{0} & \mathbf{0} \\
\mathbf{0} & \mathbf{0} & \mathbf{0} & \mathbf{0} & \mathbf{0} & \mathbf{0}
\end{bmatrix}$$

The core of the numerical solution lies in solving Eqn. 19. The equation connects the vector of spherical harmonic coefficients  $\mathbf{C}_n$  with its neighbors,  $\mathbf{C}_{n-1}$  and  $\mathbf{C}_{n+1}$ . Since the system is technically infinite  $(n \in [0, \infty))$ , a direct solution is not possible. Instead, it is solved by truncating the system at a sufficiently large integer N, which assumes that  $\mathbf{C}_{n>N} \approx 0$ . The solution strategy involves finding a series of "transfer matrices",  $\mathbf{T}_n$ , that relate each coefficient vector to the previous one, such that  $\mathbf{C}_n = \mathbf{T}_n \mathbf{C}_{n-1}$ . Substituting this relationship into Eqn. 19 allows for the isolation of  $\mathbf{C}_n$ :

$$\mathbf{Q}_n \mathbf{C}_n + \mathbf{R}_n (\mathbf{T}_{n+1} \mathbf{C}_n) = \mathbf{S}_n \mathbf{C}_{n-1}$$
$$\mathbf{C}_n = (\mathbf{Q}_n + \mathbf{R}_n \mathbf{T}_{n+1})^{-1} \mathbf{S}_n \mathbf{C}_{n-1}$$

By comparing this result with the definition  $C_n = T_n C_{n-1}$ , we find a recursive definition for the transfer matrix  $T_n$ :

$$\mathbf{T}_n = (\mathbf{Q}_n + \mathbf{R}_n \mathbf{T}_{n+1})^{-1} \mathbf{S}_n \tag{23}$$

This expression, known as a **matrix continued fraction**, allows for the calculation of  $\mathbf{T}_n$  if  $\mathbf{T}_{n+1}$  is known. To solve this, we use a numerically stable two-pass algorithm: the first pass of the algorithm computes the transfer matrices  $\mathbf{T}_n$  by working downward from the truncation index n = N. This is achieved by defining a recursive function that directly mirrors the mathematical structure of Eqn. 23. The recursion is anchored by a boundary condition at n = N, where the assumption  $\mathbf{C}_{N+1} = \mathbf{0}$  simplifies Eqn. 19 to give the starting transfer matrix  $\mathbf{T}_N = \mathbf{Q}_N^{-1} \mathbf{S}_N$ . For any n < N, the function calculates  $\mathbf{T}_n$  by recursively calling itself to find  $\mathbf{T}_{n+1}$  and then applying the matrix operations from Equation 23. Once the means to calculate any transfer matrix  $\mathbf{T}_n$  is established through this recursive definition, the second pass of the algorithm computes the actual coefficient vectors  $\mathbf{C}_n$ . This pass proceeds iteratively upward, starting from the initial condition  $\mathbf{C}_0$ , which is known from the normalization of the probability distribution function. A loop iterates from n = 1 to N. In each step, it calculates the required

transfer matrix  $\mathbf{T}_n$  using the previously defined recursive function, and immediately uses it to find the next coefficient vector via the relation  $\mathbf{C}_n = \mathbf{T}_n \mathbf{C}_{n-1}$ .

Once the coefficient vectors  $\mathbf{C}_n$  are determined, the distribution function  $W_r$  is known. The normalized in-phase (M') and out-of-phase (M'') components of the magnetization are the expectation values of the direction cosines of the magnetic moment in the rotating frame.

$$\frac{M'}{M_s} = \langle \sin \theta \cos \phi_r \rangle = \int_0^{2\pi} \int_0^{\pi} W_r(\theta, \phi_r) \sin^2 \theta \cos \phi_r \, d\theta \, d\phi_r \tag{24}$$

$$\frac{M'}{M_s} = \langle \sin \theta \cos \phi_r \rangle = \int_0^{2\pi} \int_0^{\pi} W_r(\theta, \phi_r) \sin^2 \theta \cos \phi_r \, d\theta \, d\phi_r \qquad (24)$$

$$\frac{M''}{M_s} = \langle \sin \theta \sin \phi_r \rangle = \int_0^{2\pi} \int_0^{\pi} W_r(\theta, \phi_r) \sin^2 \theta \sin \phi_r \, d\theta \, d\phi_r \qquad (25)$$

The constructed  $W_r$  is first normalized to ensure  $\int W_r d\Omega = 1$ , then the integrals are numerically evaluated after constructing  $W_r$  from the solved coefficients on a grid of  $\theta$  and  $\phi_r$ .

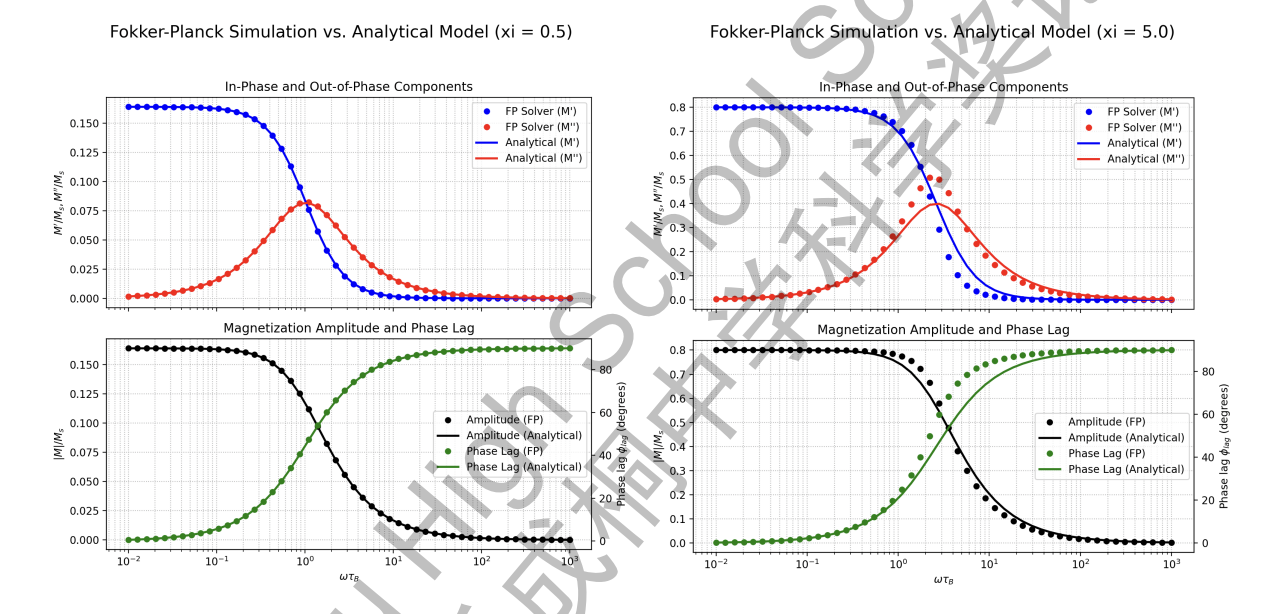


Figure 11: EFM vs Full FP Solver.

We plot the results of both models, for comparison purposes we assume Brownian-only relaxation for our FP solver too. Fig. 11 confirms the expected behavior: at low drive amplitudes the EFM matches the FP solver closely. As the field strength  $\xi$  grows the deterministic torque severely distorts  $W(\theta, \phi)$  generating higher-order harmonic modes the EFM cannot capture.

#### 4.3 Experimental Verification

We put the FP solver to the test against the linear EFM on Glycerin solutions of higher concentrations ( $\approx 30\%$  and  $\approx 60\%$ ). The results are shown below.

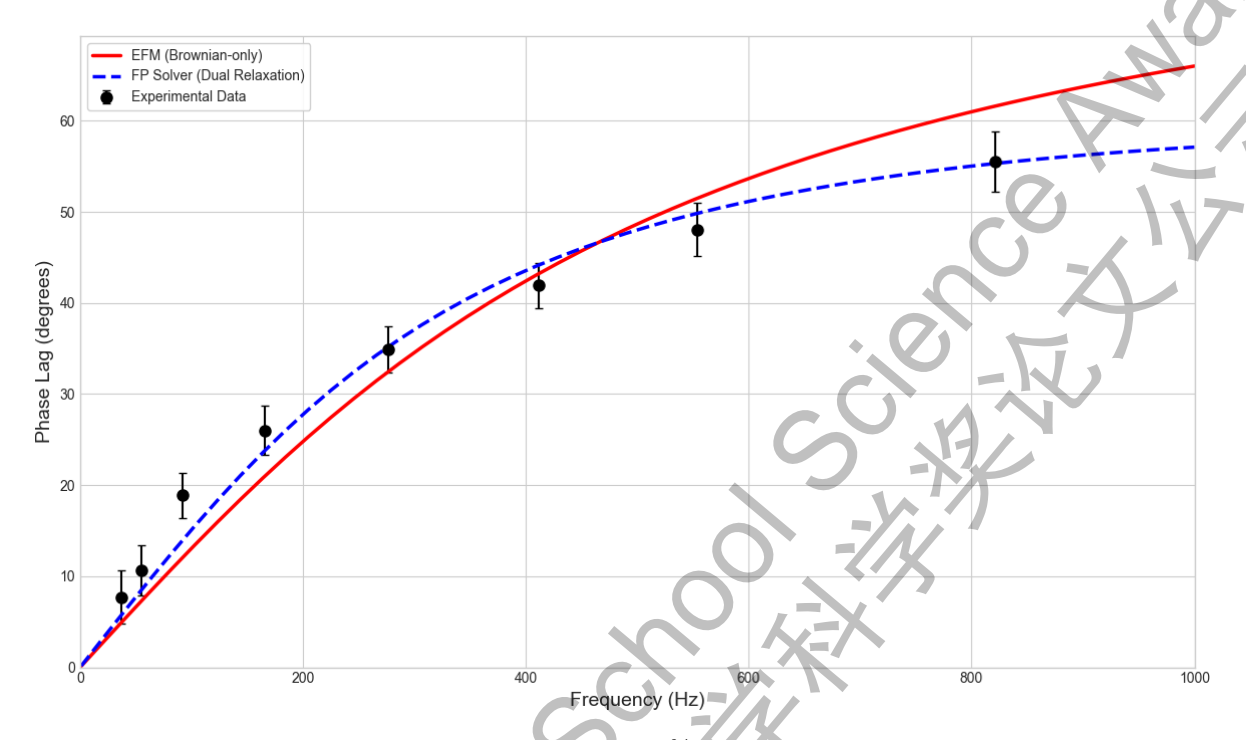


Figure 12: Phase Spectrum for 30% Dilute Glycerin Solution.

.0	EFM	FP Solver	Actual
Viscosity (mPa·s)	2.80	3.56	3.34
Fit $R^2$ Value	0.931	0.972	-

Both models reproduce the low–frequency rise of the phase in the near–linear regime, but they diverge systematically as frequency increases. The EFM progressively **overpredicts** the phase beyond  $\sim$ 480Hz, whereas the FP solver with Néel relaxation captures the earlier onset of saturation and tracks the measured curvature more closely across the upper band as shown in Fig. 12. Consistent with these shapes, the viscosity inferred by EFM is lower than that from the FP solver, with the FP solver giving a viscosity value closer to reality and a quantitatively better fit quality. Physically, the higher viscosity lengthens  $\tau_B$ , and a fraction of the polydisperse ensemble approaches the measurement timescale; the FP framework has the added Néel channel accounting for residual dispersion and includes mild field nonlinearity of Brownian rotation, thereby reducing systematic residuals at high frequency.

At a 60% concentration, the contrast between models is stronger. The EFM **overshoots** the experimental phase earlier than for 30% glycerin. In comparison, the FP solver with Néel relaxation is able to more accurately reproduce both the curvature and the high-frequency saturation more faithfully, yielding a more accurate viscosity value and a markedly higher fit quality. Most notably, the phase spectrum *plateaus earlier* than in the 30% glycerin

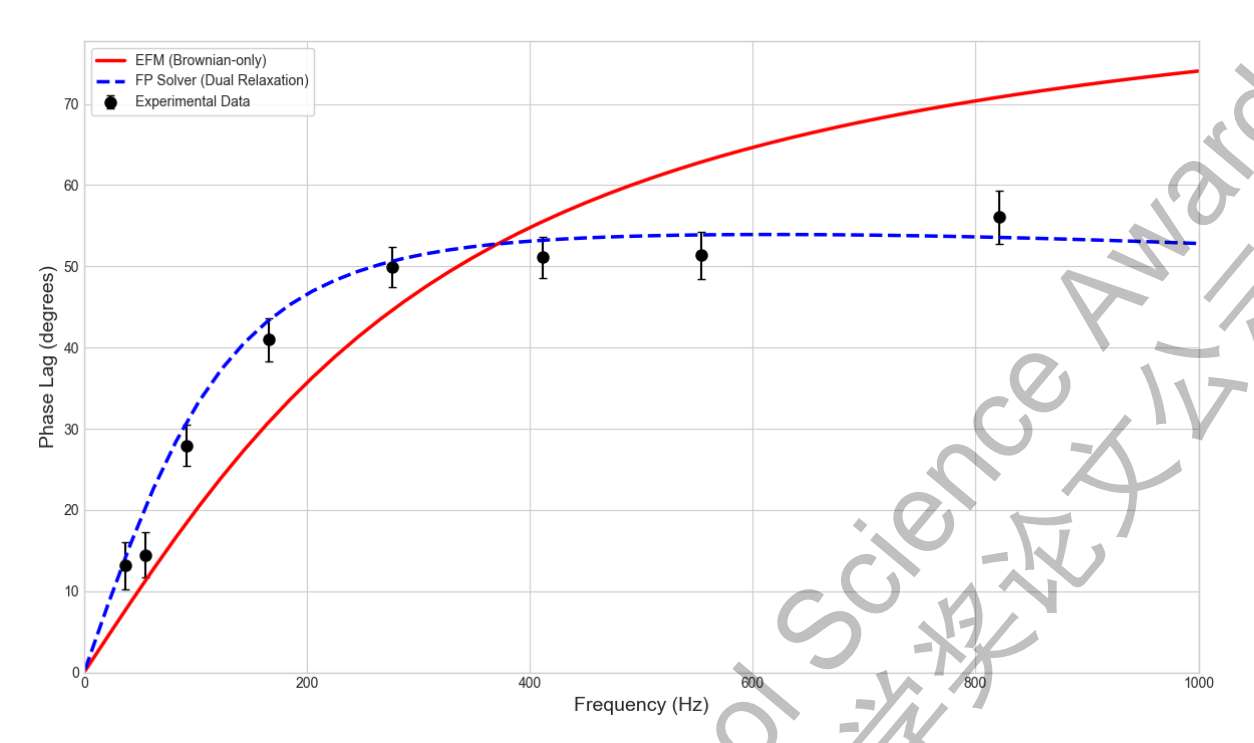


Figure 13: Phase Spectrum for 60% Dilute Glycerin Solution.

	EFM	FP Solver	Actual
Viscosity (mPas)	4.37	9.15	9.02
Fit $\mathbb{R}^2$ Value	0.699	0.969	-

sample. As the higher viscosity increases the Brownian time further, effects of Néel relaxation are more pronounced and the effective relaxation time is able to provide a better characteristic timescale for our FP solver. Polydispersity amplifies this effect (the larger- $d_h$  tail has even longer  $\tau_B$ ), and a finite Néel contribution for part of the ensemble further reduces incremental phase increase at high f. Overall, the FP +Néel framework provides parameter estimates that track concentration-dependent viscosity and delivers systematically smaller high-frequency residuals than EFM, while explaining the earlier plateau on physical grounds. We can safely conclude that this FP numerical solver framework provides greater predictive power and accuracy for more viscous solutions.

# 5 Further Applications

#### 5.1 Weighted-Average Model

Equation 9 presupposes a homogeneous particle ensemble where all particles can undergo both relaxation modes concurrently, and we consider both mechanisms in parallel to determine the effective relaxation time. However, when unconventional non-Newtonian fluids are tested, our existing models may not be adequate in describing scenarios characterized by physical inhomogeneity, something we observed in our own test samples. Such conditions arise when a fraction of the MNPs are physically immobilized, when samples of certain fluids like egg white protein have gelated, or the MNPs have aggregated into large clusters. We will explore both scenarios in more detail below. To quantitatively interpret the phase spectra, we proposed our very own Weighted-Average (WA) Model that explicitly accounts for the co-existence of two distinct MNP populations within the egg white solution, particularly during its transition into a gel. The model combines the complex magnetic susceptibility contributions from MNPs that are free to physically rotate (Brownian relaxation) and those that have been immobilized by the forming protein matrix (Néel relaxation). The total phase lag,  $\theta$ , as a function of angular frequency,  $\omega$ , is derived from these contributions:

$$\tan \theta(\omega) = \frac{rM_{\text{Brown}}''(\omega) + (1 - r)M_{\text{Neel}}''(\omega)}{rM_{\text{Brown}}'(\omega) + (1 - r)M_{\text{Neel}}''(\omega)}$$
(26)

Here, r is the crucial fitting parameter representing the fraction of nanoparticles that remain free to undergo Brownian motion. The in-phase,  $M'(\omega)$ , and out-of-phase,  $M''(\omega)$ , components for the Brownian mechanism are given by the regular Debye model [7]:

$$M'_{\text{Brown}}(\omega) = \frac{M_s L(\xi)}{1 + (\omega \tau_{\perp})^2} \quad \text{and} \quad M''_{\text{Brown}}(\omega) = \frac{\omega \tau_{\perp} M_s L(\xi)}{1 + (\omega \tau_{\perp})^2}$$
 (27)

For the immobilized particles, the Néel components are (derivation in Appendix C):

$$M'_{\rm Neel}(\omega) = \frac{M_s^2 B}{4K}$$
 and  $M''_{\rm Neel}(\omega) = \frac{M_s^2 V_c B}{k_B T \omega \tau_N}$  (28)

where K,  $M_s$ ,  $\tau_N = \tau_0 \exp\left(\frac{KV_C}{k_BT}\right)$  are the magnetic anisotropy constant, saturation magnetization, and Néel relaxation time respectively, as defined above. This WA approach is more physically sound for describing the gelation process we subsequently studied than our other theoretical frameworks. The standard Fokker-Planck solver, while fundamentally rigorous, would struggle to represent the bimodal state of a partially formed gel without immense mathematical complexity due to the assumption of a homogeneous particle ensemble where all particles undergo both relaxation modes concurrently. This strength of our new model lies in its conceptual simplicity and physical transparency, allowing us to bypass computational challenges while still extracting intuitive and meaningful parameters (r and  $\eta)$  that directly correspond to the underlying phenomena of particle immobilization and matrix stiffening.

#### 5.2 Gelation of Proteins

The thermal denaturation and subsequent gelation of an egg white protein<sup>1</sup> solution were investigated. The tubes were filled with 1ml of egg white solution and  $50\mu$ l of MNP suspension was added. The starting sample was then measured at 25C. Subsequently, the samples were immersed in a constant temperature water bath for 10 minutes to allow for the sample to heat up, after which they are cooled down and inserted back into the MIS.



Figure 14: Pictures of Egg White sample pre and post gelation.

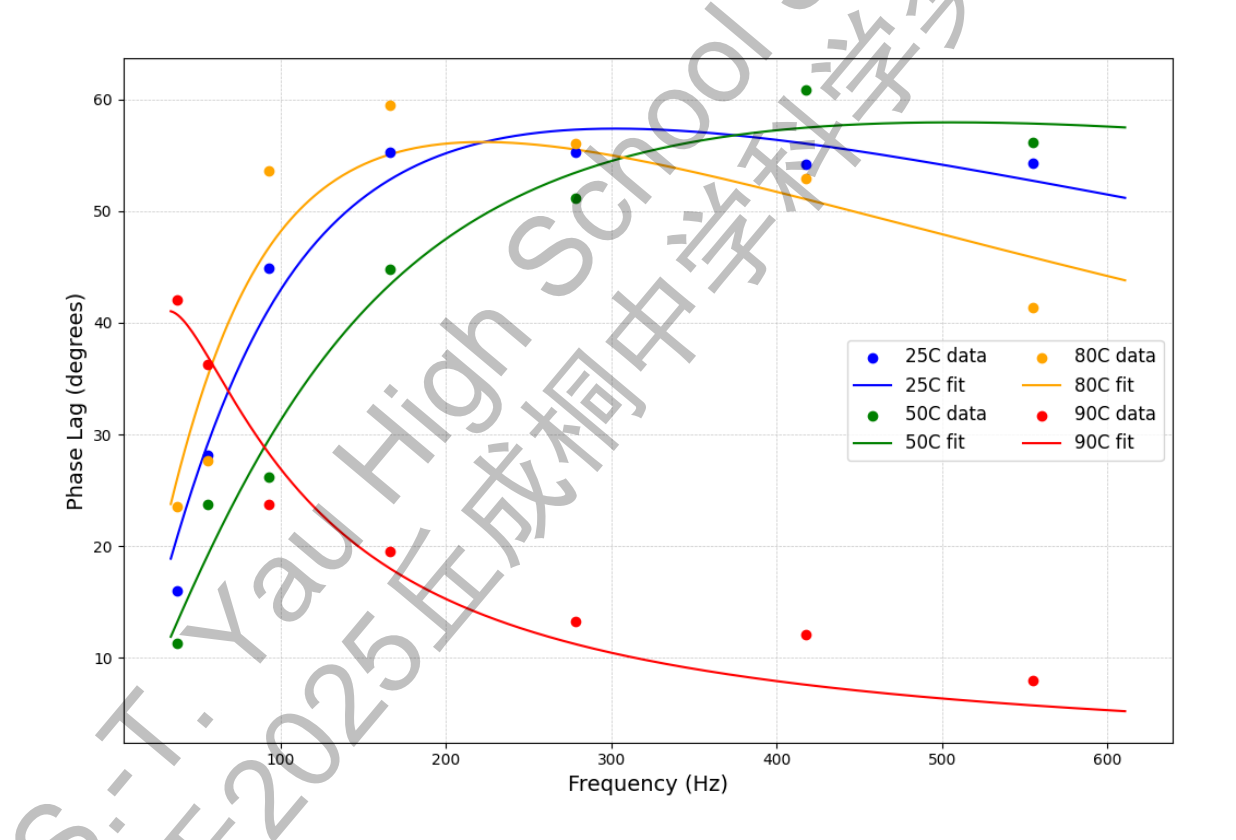
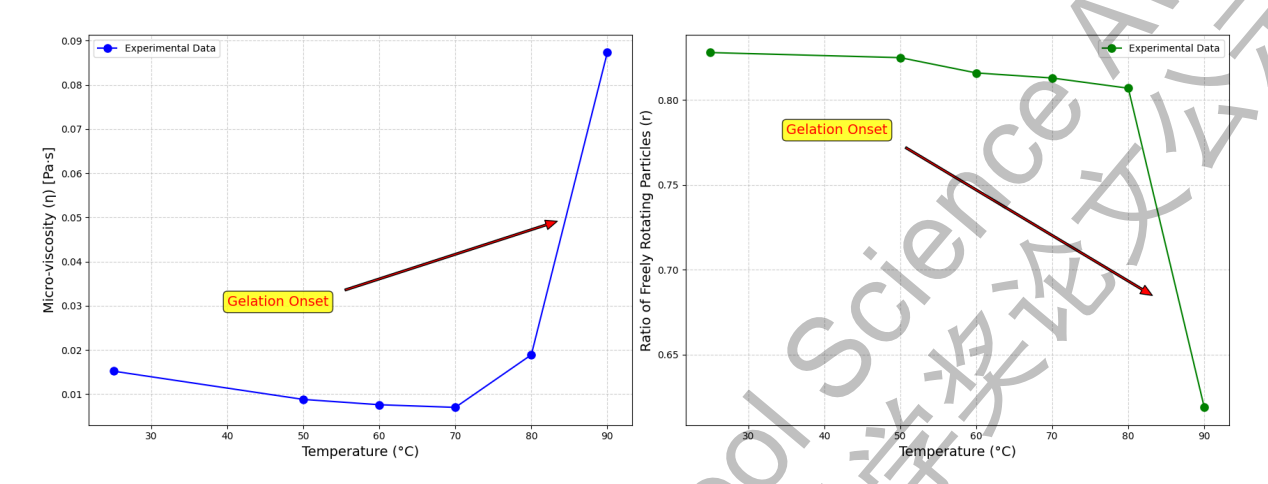


Figure 15: Phase Spectrum for Egg White solution after being heated to various temperatures.

The evolution of the phase spectra with temperature, shown in Fig. 15 (error bars omitted for easier visualization), provides a clear signature of the underlying physical transformation. Initially, the sample behaves as a viscous fluid, with phase lag curves already indicating the presence of trapped particles that undergo Néel relaxation only. As the temperature rises to 90°C, the phase spectra drastically changes – there is high phase lag at low frequencies that monotonically decreases with increasing frequency, marking the onset of **gelation**. This profile

<sup>&</sup>lt;sup>1</sup>egg white is composed of ovalbumin, ovotransferrin, ovomucoid, ovomucin, and a few other proteins.

is characteristic of a system where Brownian motion has been largely arrested due to the MNPs becoming physically immobilized within the cross-linked protein network of the formed gel, hence the magnetic response becomes dominated by the much faster Néel relaxation which is independent of the surrounding matrix. To quantify these observations, we use the WA model to fit the phase spectra using micro-viscosity  $(\eta)$  and the fraction of freely rotating particles (r).



**Figure 16:** Plots of how  $\eta$  and r change indicating gelation.

The trends of these fitted parameters against temperature, plotted in Fig. 16, provide a compelling quantitative narrative that perfectly explains the spectral changes. The initial slight decrease in viscosity from 25 to 70 °C corresponds to the fluid thinning, while the dramatic crossover event between 80 and 90 °C, where viscosity begins to increase exponentially, confirms the gelation onset. This is mirrored perfectly by a sharp drop in the fraction of free particles r from 0.807 to 0.619, which provides direct evidence that a large portion of the MNP have become trapped within the forming gel matrix. The value of r can be referred to as the porosity of the gel. We note that this value does not tend to zero most likely due to fluid-filled cavities within the gel [10]. It is important to acknowledge that the fits of the WA model to the raw spectral data are not perfect. This is an expected outcome, as our model is intentionally simplified to disregard complex phenomena such as the polydispersity of the MNPs or the non-Newtonian viscoelastic properties of the forming gel, which would require much more elaborate models with significantly higher computation times to capture perfectly [11]. Despite these simplifications, the power of this approach is undeniable. The WA model successfully deconvolves the complex phase spectra into intuitive physical parameters that provide profound qualitative and quantitative insight into the biophysical process of gelation. These findings demonstrate that magnetic impedance spectroscopy can serve as a highly sensitive, in situ probe to monitor complex structural transitions in soft matter and biological systems. This technique offers a unique window into the micro-rheological environment, capturing the transition from a simple fluid to a complex, motion-restricted gel network in a way that bulk rheology alone cannot [12].

#### 5.3 Characterization of MNPs

The other scenario in which MNPs can become immobilised is due to aggregation. We noticed this phenomenon after we ran out of commercial MNPs and tried to synthesize our own magnetite MNPs by co-precipitation. 4g of K30 PVP was dissolved in 100 mL of 2% ammonia while stirring at 700 rpm at 25°C. A precursor mix of 50 mL iron salts (1 M FeSO<sub>4</sub> and 2 M FeCl<sub>3</sub>) was added *dropwise* under continuous stirring; the solution turned black immediately, indicating magnetite formation. Stirring was continued briefly, then a permanent magnet was used to collect the particles. The supernatant was decanted and replaced with ethanol; this washing step was repeated four times to remove excess PVP, ammonia, and by-products. Finally, ethanol was exchanged for deionized water and the dispersion was stabilized with 40 mM sodium citrate to yield a purified aqueous suspension.

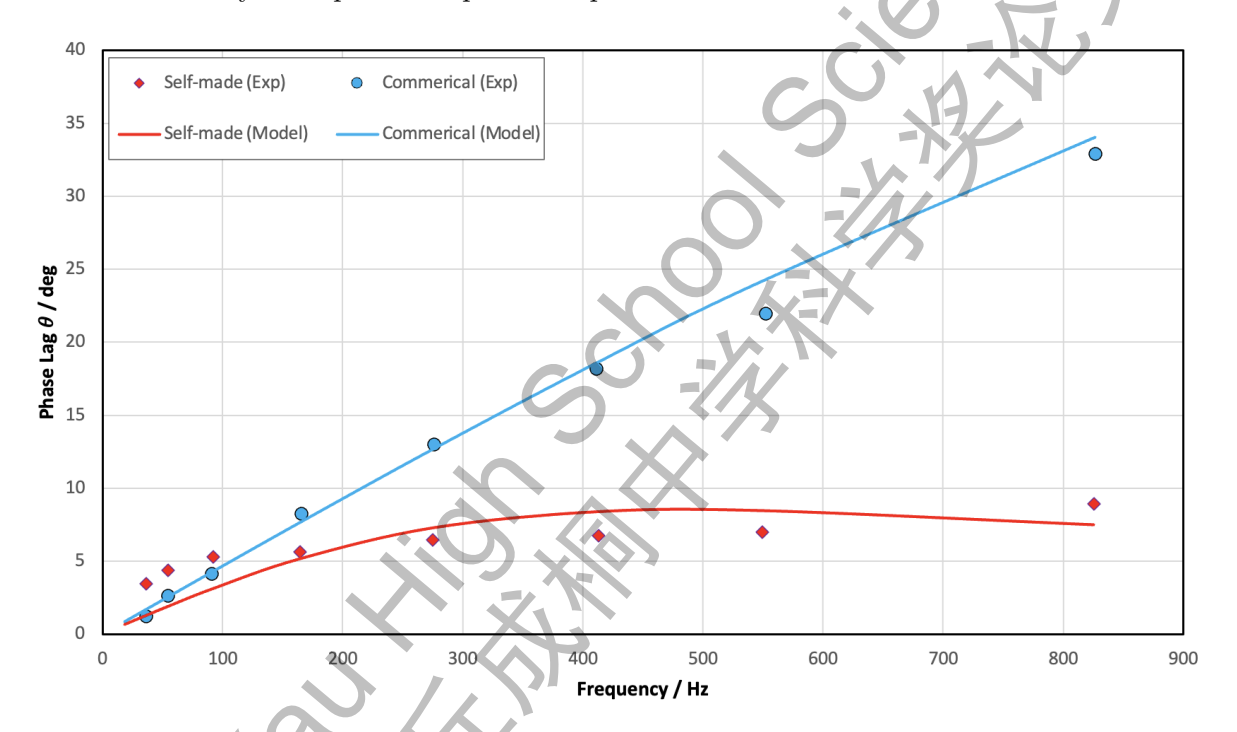


Figure 17: Phase spectrum for homemade vs commercial MNPs in distilled water.

	Homemade	Commercial
$d_H \text{ (nm)}$	102	70
r value	0.03	1.00

For MIS characterization, the homemade and commercial MNPs were each dispersed in distilled water held at the verified viscosity of  $0.95\,\mathrm{mPa}\cdot\mathrm{s}$  (logged at room temperature). For this test, viscosity was fixed to this standard value for the WA model and we fitted hydrodynamic volume  $V_h$  together with the mobility fraction r. The homemade sample exhibited a spectrum with a steep low-frequency rise followed by an early plateau, consistent with a Néel-dominated response. Quantitatively, the WA fit returned a visually good fit for the commercial MNPs with r=1 indicating no trapped particles, while for our own MNPs it returned a very small mobile fraction,  $r_{\mathrm{new}}=0.03$ , and a much larger hydrodynamic diameter  $d_h\approx 102\,\mathrm{nm}$ .

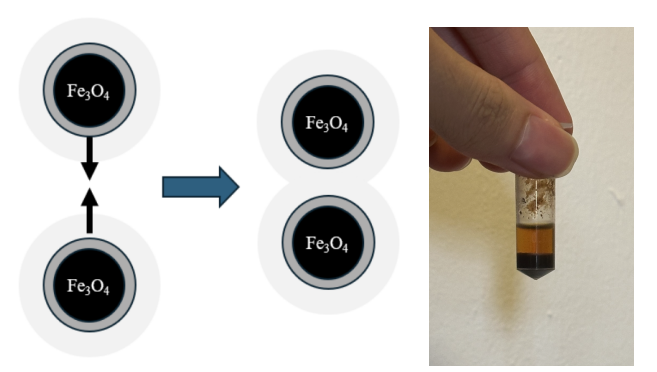


Figure 18: Illustration of aggregation of homemade MNPs during synthesis process.

We attributed this peculiar behavior to aggregation of our homemade MNPs. When a nanoparticle suspension is well dispersed, it stays evenly cloudy for a long time: the particles are tiny, Brownian motion keeps them mixed, and they are too light to settle. For our sample containing homemade MNPs (Fig. 18), a clear top layer and a dark blob appear after a few hours. This is characteristic of aggregation: particles stick together into bigger clumps, which are heavier and fall to the bottom, leaving the liquid above clearer. Clumping of MNPs can happen if the surface coating of PVP (polyvinylpyrrolidone) is overloaded and particles sitck together. Either way this alludes to a poorly controlled synthesis process, and the sedimentation we see supports the aggregation explanation and is consistent with our MIS results, which show a small mobile fraction and more Néel-like (trapped) behaviour. However, these findings reinforce the role of the heuristic WA model as a practical descriptor for complex samples in which a subset of particles is mechanically hindered. In our gelation experiments, r(T) decreased as a percolated network formed; here, aggregation drives the same phenomenology:  $r \ll 1$  and an inflated  $V_h$ capture the loss of whole-particle rotation without requiring additional ad hoc parameters. Operationally, fitting  $\{V_h, r\}$  with the viscosity fixed to a distilled-water standard could possibly provide a rapid quality-control readout: large inferred  $V_h$  together with small r flags agglomeration, whereas smaller  $V_h$  and larger r indicate a predominantly Brownian, well-dispersed suspension.

This technique is also useful for manufacturers to quantify the magnetic properties of their MNPs on-site, on top of the size distribution of the MNPs as shown in Appendix B.

# 6 Conclusion

In conclusion, we engineered a Magneto-Impedance Spectrometer from the ground up, incorporating custom electronics from start to finish (generating the driving field to finally extracting phase lag). Our results show that the system can reliably generate uniform rotating magnetic fields, achieve low harmonic distortion, and control temperature appropriately. By integrating a theoretical framework that accounts for high field/frequency nonlinearities, dual relaxation mechanisms and particle size distribution, we improved fit quality drastically for Glycerin solutions across a range of viscosities. Experimental trials on gelating egg white solution confirmed that MIS can sensitively track viscosity changes and accurately identify gelation temperatures, for which we derived and fitted an original Weighted Average Model to give us quantitative insight. These findings demonstrate that magnetic impedance spectroscopy is not only a powerful analytical tool for fundamental soft-matter research but also holds heavy practical promise.

# **Epilogue**

The next step forward is to merge the phase-lock function into the same processor that generates the driving signals; this will solidify MIS as an even more compact and cost-effective device.

One immediate and significant application of the MIS is addressing the pressing issue of substandard and falsified IV fluids causing thousands of preventable deaths annually. According to studies, over 10% of medical products in developing countries are fake [13]. Current verification methods consist of laboratory testing (\$500-2000, 3-7 day turnaround), osmometers (\$5,000-15,000, requires trained technicians), and refractometers (limited to refractive index), which are impractical for routine screening due to high cost, requiring trained personnel and lack of portability. The MIS can potentially revolutionize IV fluid verification through its unique advantages: small sample requirement enables sterile testing directly from IV ports and the low cost of production makes widespread deployment feasible. Critically, IV fluids are ideal test subjects as Newtonian fluids with well-defined viscosities [14], which work well for our instrument.

The demonstrated ability of our MIS to accurately pinpoint gelation temperatures also opens promising avenues in the food industry, where precise control of gel formation is critical to product texture, stability, and safety. Many food products—such as dairy gels, confectionery, and plant/animal-based protein gels require tight temperature monitoring during processing to achieve consistent rheological properties. By enabling in situ, non-destructive monitoring of the gelation process, MIS could serve as a valuable quality control tool, reducing reliance on slower bulk rheometry methods and allowing real-time adjustment of production parameters [12].

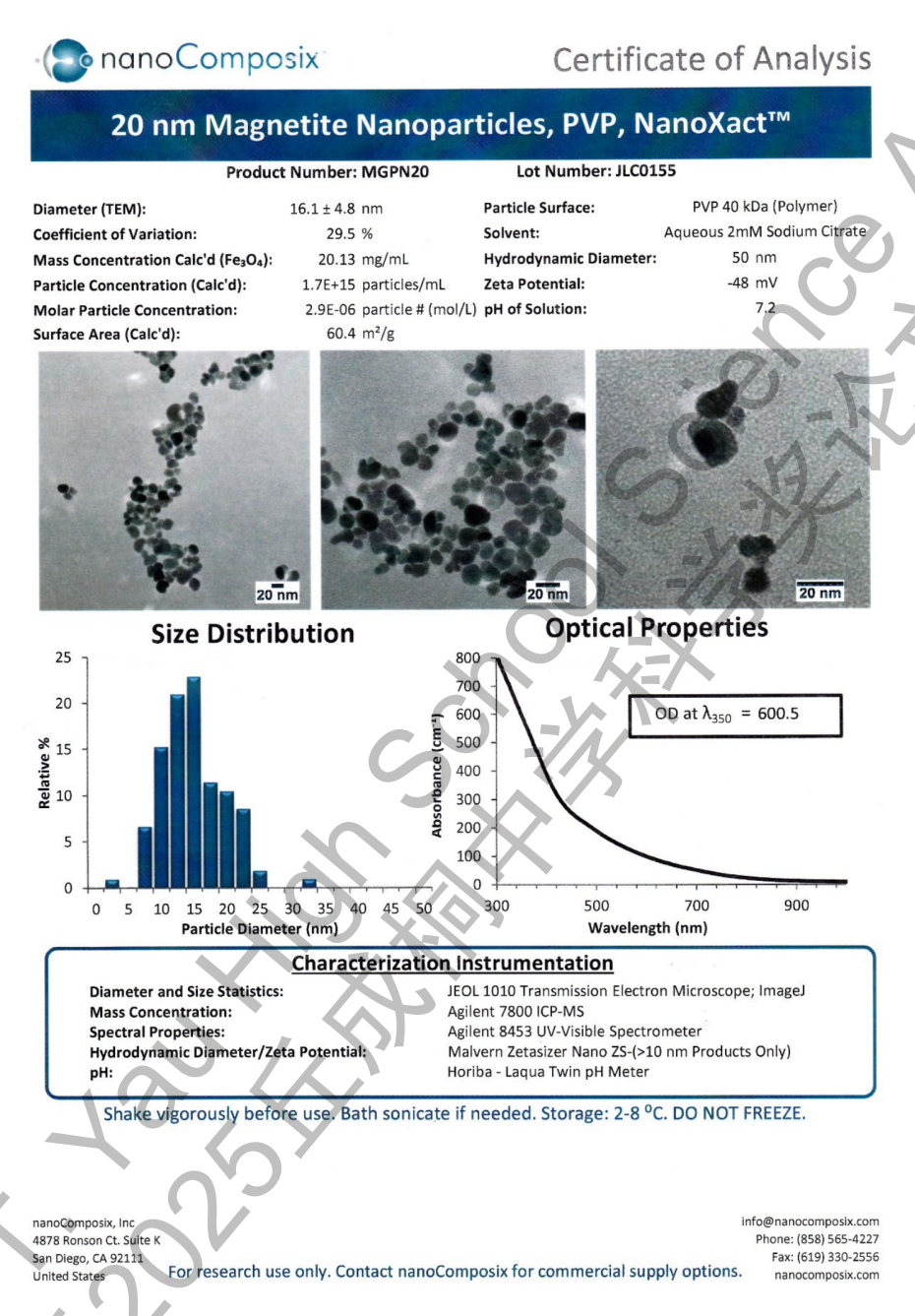
# References

- [1]: Shukla et al. (2024) Green magnetic nanoparticles: a comprehensive review of recent progress in biomedical and environmental applications in Journal of Material Sciences. DOI: 10.1007/s10853-023-08914-5
- [2]: Berret (2016) Local viscoelasticity of living cells measured by rotational magnetic spectroscopy in Nature Communications. DOI: 10.1038/ncomms10134
- [3]: Dieckhoff et al. (2011) Fluxgate based detection of magnetic nanoparticle dynamics in a rotating magnetic field in Applied Physics Letters. DOI: 10.1063/1.3639276
- [4]: Pal et al. (2022) Extending depolarized DLS measurements to turbid samples in Journal of Colloid and Interface Science. DOI: 10.1016/j.jcis.2022.06.113
- [5]: Büchner et al. (2025) Wide-field spectroscopic imaging of optical activity in Nature Photonics. DOI: 10.1038/s41566-025-01722-0
- [6]: Douglas Self (2008) Distortion in power amplifiers, Part V: output stages in EDN Journal.
- [7]: Yoshida et al. (2012) -Magnetic fluid dynamics in a rotating magnetic field in Journal of Applied Physics. DOI: 10.1063/1.3688254
- [8]: Radnik et al (2022) Composition, thickness, and homogeneity of the coating of core-shell nanoparticles—possibilities, limits, and challenges of X-ray photoelectron spectroscopy in Analytical and Bioanalytical Chemistry. DOI: 10.1007/s00216-022-04057-9
- [9]: Reeves and Weaver (2015) Comparisons of characteristic timescales and approximate models for Brownian magnetic nanoparticle rotations in Journal of Applied Physics. DOI: 10.1063/1.4922858
- [10]: Somaratne et al. (2019) Food Hydrocolloids. DOI: 10.1016/j.foodhyd.2019.105258
- [11]: Mine, Y. (1995). Recent advances in the understanding of egg white protein functionality in Trends in Food Science & Technology.
- [12]: Strasberg, E. (2000) Probing gelation with magnetic nanorods: A microrheological approach in the Biophysical Journal, 78(5), 2582-2587. DOI: 10.1016/S0006-3495(00)76737-4
- [13]: Kelesidis et al. (2019) in The Lancet. DOI: 10.1016/S0140-6736(19)30032-0
- [14]: Biomechanics: Circulation by Y.C. Fung (1997) (2nd edition, Springer)
- [15]: Mahabadi, H. K., & Rudin, A. (1979) Effect of Solvent on Concentration Dependence of Hydrodynamic Volumes and GPC Elution Volumes in Polymer Journal, 11, 123–131. DOI: 10.1295/polymj.11.123

7//-

# **Appendices**

#### Appendix A: MNP Specifications



In our modeling, the hydrodynamic volume  $V_h$  was not taken directly from the manufacturer's specification sheet, as prior studies have shown that  $V_h$  can vary significantly between different solvent environments due to changes in the bound solvent layer and interfacial effects [15]. To determine an appropriate  $V_h$  for our experimental conditions, we performed a calibration run using a reference sample of distilled water with a verified viscosity of 0.95 mPa·s. We fitted the single free parameter of shell thickness t in our polydisperse effective field model (EFM), keeping all other parameters fixed, to match the measured phase spectrum for this reference sample. This yielded a best-fit shell thickness of t = 26 nm, which we subsequently applied in all blind tests on other distilled water and glycerin solutions.

#### Appendix B: Error Propagation due to Thermal Fluctuations

We roughly estimate the influence of temperature drift and thermometer accuracy on the measured phase lag using our theoretical model presented in Section 3.1:

$$\phi(\omega) = \arctan(\omega \tau)$$

where for Brownian relaxation,

$$\tau = \frac{3\eta V_h}{k_B T}$$

Thus  $\tau \propto \eta/T$ , and the derivative of  $\phi$  with respect to T is

$$\frac{\partial \phi}{\partial T} = \frac{\omega \tau}{1 + (\omega \tau)^2} \left( \frac{1}{\eta} \frac{\partial \eta}{\partial T} - \frac{1}{T} \right)$$

The prefactor  $\frac{\omega \tau}{1+(\omega \tau)^2}$  is maximised at  $\omega \tau=1$ , with a value of 1/2. At room temperature  $(T\approx 298~\mathrm{K}),\,1/T\approx 3.36\times 10^{-3}~\mathrm{K}^{-1}$  (0.336%/°C), and a conservative estimate for the viscosity slope is

$$\frac{1}{\eta} \frac{\partial \eta}{\partial T} \approx -3.0 \times 10^{-2} \text{ K}^{-1} \quad (-3\% \text{ per } ^{\circ}\text{C})$$

In the worst-case at  $\omega \tau = 1$ :

$$|\Delta\phi|_{\text{max}} \approx \frac{1}{2} |-0.0300 - 0.00336| \Delta T = 0.01668 \Delta T \quad \text{(rad)}$$

For the observed 10-min run the temperature drift was  $\Delta T = \pm 0.3$ °C:

$$|\Delta\phi|_{\rm max} \approx 0.0050 \ {\rm rad} \approx 0.29^{\circ}$$

The thermometer accuracy reported by the manufacturer is  $\pm 1.0^{\circ}$ C (systematic error), thus the total uncertainty in  $\Delta T$  in quadrature is

$$\Delta T_{\rm tot} \approx \sqrt{1.0^2 + 0.3^2} \approx 1.04^{\circ} \text{C}$$

giving a maximum phase lag error of

$$|\Delta\phi|_{\rm max} \approx 0.0174 \ {\rm rad} \approx 1.0^{\circ}$$

Therefore, the worst-case temperature-induced phase uncertainty is  $\lesssim 1^{\circ}$  at the relaxation peak, and smaller elsewhere. We can thus use a constant T assumption with confidence in our model's predictive power.

# Appendix C: Néel Response of Immobilized Particles (Derivation for the WA model)

We consider a dilute ensemble of uniaxial, single-domain MNPs with isotropically distributed easy-axis directions. The particles are assumed to be immobilized and driven by a small sinusoidal field  $B(t) = B \sin \omega t$ . We work in the linear, small-tilt regime. Demagnetizing fields, interparticle interactions, and field-induced barrier lowering beyond first order are neglected.

Let the angle  $\gamma$  be the small tilt of the magnetic moment from the easy axis under field B. From torque balance in a uniaxial anisotropy well, the geometry leads to

$$\tan \gamma = \frac{M_s B \sin \varphi}{2K \cos \varphi + M_s B \cos \varphi} \tag{29}$$

where K is the anisotropy energy density and  $\varphi$  is the angle between the field and the easy axis. In the low–field, small–angle limit  $(B \ll K/M_s, \gamma \ll 1)$ ,

$$\gamma = \frac{M_s B \sin \varphi}{2K} \tag{30}$$

The in-phase magnetisation increment is obtained by averaging over all easy-axis orientations:

$$M' = M_s \int_0^{\pi} \gamma(\varphi) \sin \varphi \, d\varphi = M_s \int_0^{\pi} \frac{M_s B}{2K} \sin^2 \varphi \, d\varphi \tag{31}$$

Thus the trapped, in-phase contribution used in the weighted-average (WA) model is

$$M'_{\rm N\acute{e}el}(\omega) = \frac{M_s^2 B}{4K}$$

The equation for out-of-phase signal originates from Néel switching over the barrier KV, where V is the core volume of the particle. In Boltzmann theory the switching rate is the product of the attempt frequency f and the Arrhenius factor:

$$\Omega = f e^{-\Delta E/k_B T} \tag{32}$$

In a weak field, the forward and backward barriers are  $\Delta E_{\pm} = KV \mp M_s V B$  (taking B along the easy axis). Expanding the corresponding rates and summing the two directions gives

$$\Omega = f \left[ e^{-(KV - M_s V B)/k_B T} - e^{-(KV + M_s V B)/k_B T} \right] 
= f e^{-KV/k_B T} \left( e^{+\xi} - e^{-\xi} \right) \approx 2f e^{-KV/k_B T} \xi = 2f e^{-KV/k_B T} \frac{M_s V B}{k_B T}$$
(33)

in small field limit ( $\xi \ll 1$ ). Averaging over random orientations of the easy-axis introduces a factor 1/2, yielding the working form

$$\Omega = f e^{-KV/k_B T} \frac{M_s V B}{k_B T} = \frac{1}{\tau_N} \frac{M_s V B}{k_B T}$$
(34)

The thermal switching produces a time derivative of the magnetisation proportional to  $\Omega$ 

$$\frac{\partial M}{\partial t} = M\Omega \tag{35}$$

which is valid in the high-frequency limit  $\omega \tau_N \gg 1$ , while the magnetization vector cannot catch up to the external sinusoidal field  $B(t) = B \sin \omega t$ . The out-of-phase part of the response thus scales as

$$M'' = \frac{M_s \Omega}{\omega}. (36)$$

Substituting  $\Omega$  above and writing  $V \equiv V_c$  as the core volume gives the compact result used in our WA model:

$$M_{\text{N\'eel}}''(\omega) = \frac{M_s^2 V_c B}{k_B T \, \omega \tau_N}$$

These two expressions provide, respectively, an in–phase contribution and a  $1/\omega$  quadrature contribution for the immobilised Néel particles. In the WA model, they are combined with the Brownian branch of freely rotating particles, whose Debye–like peak supplies the complementary frequency dependence needed for robust separation of the free fraction and micro-viscosity during gelation.